A Free-Standing Molecular Spin–Charge Converter for Ubiquitous Magnetic-Energy Harvesting and Sensing

*Beibei Xu, Himanshu Chakraborty, Richard C. Remsing, Michael L. Klein, and Shenqiang Ren**

Self-powered organic conjugated materials are of vital importance for the development of next-generation, flexible, and fully integrated energy, sensing, and artificial-intelligence technologies. Due to their exceptionally long spin lifetimes and strong spin–charge interactions, these carbon materials could also impact data transmission, processing, and storage. However, to exploit these opportunities, the ability to directly convert energy from spin information to electric charge is essential. Here, we introduce a novel molecular spin–charge converter that is comprised of a centimeter-sized free-standing organic charge-transfer crystal. Magnetic-field effects in this material induce intersystem crossings and spin–charge-lattice couplings that generate an electric voltage for magnetic-energy harvesting. The effective conversion between charge and spin stimulus permits simultaneous and instantaneous self-powering and sensing performance in a molecular crystal that displays anisotropic behavior dependent on crystal orientation. We confirm the strong charge-transfer character of the crystals with first principle calculations of the electronic density of states. The solution processed flexible devices also exhibit an excellent temperature sensitivity of <0.01 K and a unique piezoresistance coefficient of -5.1×10^{-6} Pa^{-1}. The self-powered sensing performance of this molecular spin–charge converter, together with its solution processability and flexibility, endow this molecular charge-transfer crystal with the capability to drive a new generation of noncontact magnetic-energy harvesting and sensing technologies.

A spin–charge converter is an energy harvesting and multisensing material that converts spin information (magnetic energy) into electrical energy, and transduces multiple stimuli into a coupled signal. These materials play a vital role in the development of micro/nanosystems for next-generation artificial intelligence, personal healthcare systems, and more.[1] Over the past decades, numerous organic-based materials have been evaluated for their use in energy harvesting applications from sources present in the environment, due to their electrostatic, optoelectronic, electromagnetic, piezoelectric, or magnetoelastic origin.[1,2] Currently, one of the most rapidly developing technologies is energy harvesting and sensing from the magnetic field of the earth, human brain and heart, and high-voltage power lines. The magnetic energy shows comparative advantages due to its ubiquitous distribution from the environment and noncontact capture through the use of magnetoelectric materials.[3] Traditionally, energy harvesting and sensing of magnetoelectric materials are based on the combination of inorganic magnetostrictive and piezoelectric materials, enabling the capture of a magnetic field as small as 10^{-12} T at a frequency as low as 10^{-2} Hz.[4] Despite these achievements, it still remains a challenge to develop solution processed, flexible, self-powered magnetic-energy-harvesting devices with multisensing functions. By contrast, organic materials show great promise in the development of all-organic energy harvesting and smart sensing systems because they are lightweight, flexible, and solution processable. In this context, it is in urgent demand for the development of organic materials with magnetic-energy harvesting and sensing ability.

Unique multifunctional responses of organic charge-transfer (CT) materials have been demonstrated because of the exchange interaction induced by charge–spin coupling and the delocalized π-electrons endow organic CT complexes with magnetoelectric properties.[5] Widespread application of these fascinating multifunctional CT crystals has been limited because the critical requirement of external power supplies impedes their use in dual-functional energy harvesting and sensing.[6] Pioneering work using κ-(BEDT-TTF)$_2$Cu[N(CN)$_2$]Cl (BEDT-TTF = bis(ethylenedithio)tetrathiafulvalene) CT crystals started the field of organic CT multiferroicity.[7] Moreover, strain-induced superconductor–insulator conversion has been reported in κ-(BEDT-TTF)$_2$Cu[N(CN)$_2$]Cl crystals with a minor strain smaller than 1%, highlighting the promising mechanoelectric applications of BEDT-TTF based CT crystals.[8]

Despite these advances, magnetic-field energy harvesting has not yet been observed in these organic CT materials. More importantly, the power generation of organic materials (self-powered) can facilitate flexible sensors with ultralow power consumption. This is particularly attractive because organic materials can therefore simultaneously harvest magnetic energy and sense external stimuli quantitatively. The

Dr. B. Xu, Prof. S. Ren
Department of Mechanical Engineering and Temple Materials Institute
Temple University
Philadelphia, PA 19122, USA
E-mail: shenqiang.ren@temple.edu
Dr. H. Chakraborty, Dr. R. C. Remsing
Department of Chemistry and Center for the Computational Design of Functional Layered Materials
Temple University
Philadelphia, PA 19122, USA
Prof. M. L. Klein
Department of Chemistry
Center for the Computational Design of Functional Layered Materials, and Temple Materials Institute
Temple University
Philadelphia, PA 19122, USA

DOI: 10.1002/adma.201605150

materials-by-design freedom afforded by widespread donor–acceptor combinations and unique stacking arrangements, in addition to multiple degrees of CT, enables organic CT materials with multifunctionalities, in contrast to unipolar molecules.[9] By virtue of these advantages, $(BEDT\text{-}TTF)_2C_{60}$ CT crystals (BCCTs) have been selected as the prototypical example to realize energy harvesting and multisensing functionality. In general, the growth of high-quality BCCT single crystals of uniform structure is a prerequisite for the investigation of their crucial spin–charge properties and structure–property relationships. However, the large structural and solubility differences between the BEDT-TTF electron donor and C_{60} acceptor impedes their cocrystallization into uniform single-crystal structures of large dimension and high yield.

In this work, we present a strategy for the controlled growth of BCCT crystals and demonstrate their ability to simultaneously perform magnetic-field energy harvesting and respond to external stimuli. The functional properties of these crystals are then rationalized through the nature of their charge-transfer process using experimental measurements and quantum mechanical density functional theory (DFT) calculations.

Herein, we adapt a modified chemical bath deposition strategy combined with a solvent evaporation method for the control and growth of high-quality BCCT single crystals (**Figure 1**a). In consideration of the solubility of these molecules and the polarity of the solvent, a controlled evaporation rate facilitates the formation of supersaturated solution with the separated nucleation and growth into free-standing centimeter-sized long and several hundred micrometer wide crystals (Figure 1b,c). The elemental mapping of energy dispersive X-ray spectroscopy confirms the coexistence of these molecules in the crystals (the inset of Figure 1c and Figure S1 (Supporting Information)). It should be noted that a very slow or fast evaporation rate can prevent growth or lead to fast nucleation into a bundle of randomly distributed small crystals (Figure S2, Supporting Information). The effect of temperature and concentration on the growth of BCCT crystals was also investigated as shown in Figure S4 and S5 in the Supporting Information.

The X-ray diffraction (XRD) pattern of BCCTs is shown in Figure 1d. The unit cell contains eight molecules of BEDT-TTF and four molecules of C_{60}, where BCCTs are packed in monoclinic structure with the lattice constant $a = 25.87$ Å, $b = 21.87$ Å, $c = 9.91$ Å, and $\beta = 105.13°$ (Figure 1e), and the CT interaction occurs between a C_{60} molecule and its six adjacent BEDT-TTF molecules (single-crystal diffraction data of BCCTs were collected at 100 K with a wavelength of 0.8 Å on a SER-CAT 22-BM beamline at the Advanced Photon Source in the Argonne National Laboratory). The separation of sulfur atoms from BEDT-TTF and carbon atoms of C_{60} ranges between 3.43 and 3.49 Å. The distance between the carbon atoms of BEDT-TTF and C_{60} ranges from 3.17 to 3.39 Å. The intermolecular distance of carbon atoms for C_{60} molecules is 3.28 Å. Our DFT calculations predict values of 3.45, 3.25, and 3.25 Å, respectively, for these three distances, supporting the accuracy of our models used to later examine the charge-transfer process.

The π–π conjugation interaction in BEDT-TTF and C_{60} molecules is along the crystal growth direction (c axis). The anisotropic packing structure enables the crystals to show anisotropic optoelectronic properties (Figure 1f,g), in which the in-plane and out-of-plane measurements are along the horizontal and vertical to the crystal growth direction, respectively. Current-density–electric field (J–E) curves under dark and AM-1.5 solar illumination (20 mW cm^{-2}) of BCCTs exhibit diode behavior with superior photodetector performance, while the horizontal orientation possesses much higher performance than that of the vertical orientation due to the preferred π–π stacking direction for a large charge density with high mobility and the shorter distance of adjacent C_{60} molecules and BEDT-TTF molecules, which facilitates electron and hole hopping. The ohmic region of the J–E curves under dark is examined to obtain the horizontal and vertical conductivity of 5.30×10^{-11} and 2.53×10^{-11} S m^{-1}.[10] The iodine doping of BCCTs results in the conductivity increase to 3.91×10^{-10} and 1.91×10^{-10} S m^{-1} for horizontal and vertical orientations, respectively (the inset of Figure 1f).[11] The dissociation of photogenerated carriers can increase the current density of the horizontal and vertical orientations, which exhibit photoconductivity with an on/off ratio of 4 and 1.8, respectively.

In order to demonstrate a proof-of-principle magnetic-energy harvesting and sensing of BCCTs, the free-standing crystals are integrated into the device and contacted by two sets of electrodes for the horizontal and vertical measurements. A Helmholtz coil with the output ac magnetic field of 0.5 Hz was used for the magnetic-field energy harvesting and sensing study of BCCTs (**Figure 2**a,b). Under an oscillating magnetic field of 2000 Oe (Figure 2a), the horizontal orientation of the BCCT crystal generates an output current of ≈62 pA and voltage of ≈67 μV, while the vertical orientation gives an output current of ≈19 pA and voltage of ≈49 μV without the loading of external voltage (Figure 2c,d and the insets). Peaks in the current signal are recorded when the magnetic field is turned on and off, while the power harvesting and the magnetic field oscillate in phase (Figure 2a–d). The generated current and voltage show a near-linear relationship with an increase of external magnetic field, and the horizontal orientation exhibits a larger magnetic-energy harvesting performance than that of the vertical orientation (Figure 2e). Moreover, electric voltage generation for both orientations of BCCTs can be further enhanced under photoexcitation with an output current and voltage of ≈98 pA and ≈75 μV along the horizontal orientation at a light intensity of 120 mW cm^{-2} under a magnetic field of 2000 Oe, in which an optimum magnetoelectric coupling coefficient of ≈3.12 μV cm^{-1} Oe^{-1} is achieved (Figure 2f). The calculated power density equals to 4×10^{-12} μW Oe^{-2} cm^{-3} along this orientation. Consistent with the above discussion of Figure 1f,g, a higher charge density along the π–π stacking direction (horizontal orientation) enables a superior and anisotropic magnetic-energy harvesting performance, and thus a higher voltage is observed in the horizontal direction than that of the vertical orientation. The magnetoelectric coefficient and power density of BCCT materials are resulted from the unique charge–spin-lattice coupling of molecular charge-transfer crystals, in which magnetic energy conversion mechanism is drastically different from that of magnetoelectric oxide counterparts.[4,12]

An intriguing question is whether intermolecular radicals and excitation processes play an important role for magnetic-energy harvesting in BCCT materials.[13] Magnetic-field effects are critical to reveal and elucidate charge-transfer controlled

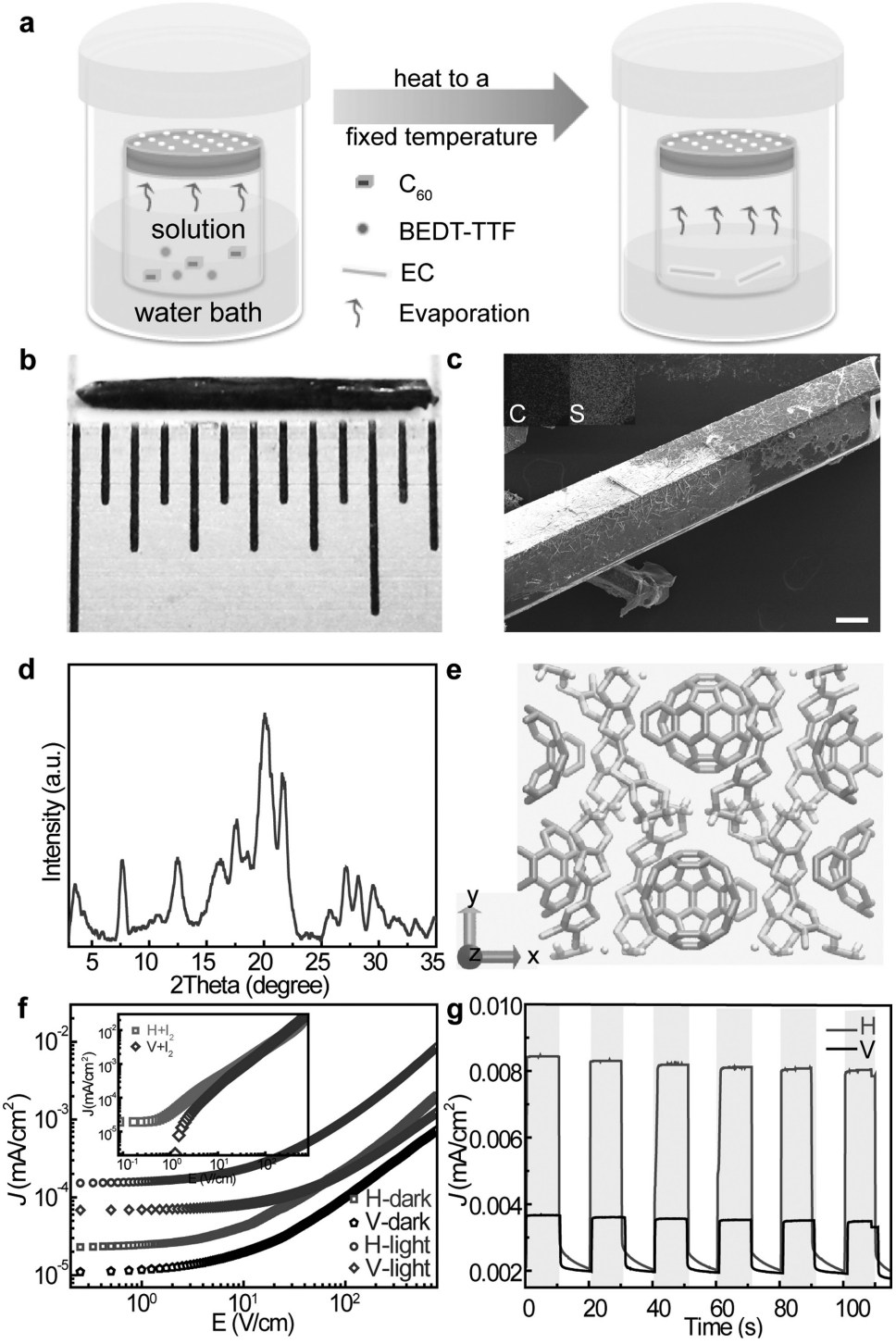

Figure 1. a) Growth scheme of $(BEDT\text{-}TTF)_2C_{60}$ charge-transfer crystals (BCCTs). Modified chemical-bath deposition combined with solvent evaporation methods was used. b) Optical microscopy image of centimeter-sized BCCTs. c) Scanning electron microscopy images of BCCTs. The inset shows the element mapping for carbon and sulfide elements by energy dispersive X-ray spectroscopy. d) Single-crystal X-ray diffraction pattern of BCCTs. e) Packing structure of BCCTs. f) Current-density–electric-field curves for BCCTs of horizontal (H) and vertical (V) orientations under dark and AM-1.5 light source with a power of 20 mW cm^{-2}. The inset is the current-density–electric-field curves for BCCTs of horizontal and vertical orientations by iodine doping. g) Photoresponse for horizontal and vertical orientations.

intermolecular radicals and excited processes in BCCTs,[14] where the external magnetic field can induce the spin mixing of singlet and triplet CT, and leads to the change of polarons and triplet excitons.[15] The BCCTs exhibit magnetic-field-dependent capacitance in which the magnetic field and capacitance oscillate in phase (**Figure 3**a).[16] Anisotropic magnetocapacitance

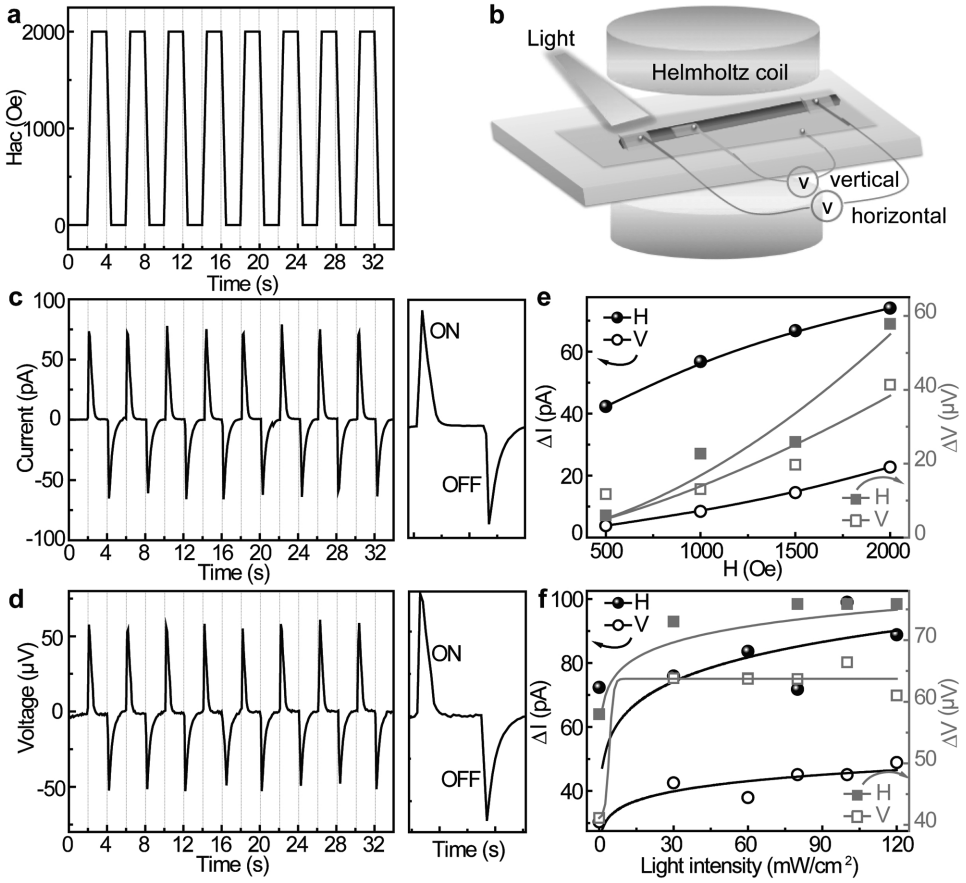

Figure 2. a) Measurement scheme of magnetoelectric coupling with the generation of current and voltage for horizontal and vertical orientations. b) Frequency-dependent external magnetic-field change. c,d) The generation of current and voltage without the loading of external voltage at a magnetic field of 2000 Oe. The right insets are the enlarged figures. e) Magnetic-field-dependent generation of current and voltage for horizontal (H) and vertical (V) orientations. f) Light-intensity-dependent generation of current and voltage for horizontal and vertical orientations.

is observed in the horizontal and vertical directions of BCCTs, suggesting the origin for the anisotropic voltage generation in BCCTs (Figure 3a,b). As the external magnetic field induces intersystem crossing for the conversion of singlet CT to triplet CT in BCCTs, the exchange interaction and spin–charge-lattice coupling generates a flow of spins (spin current) in the long-range ordered BCCTs, which, in turn, induces an electric field perpendicular to the spin current and magnetic field direction (Figure 3c). According to our measurement scheme, the direction of the generated electric field is along the horizontal orientation of BCCTs. Moreover, photoexcitation can change the density of triplet excitons to control the dipole density (the inset of Figure 3b). The increase of light intensity for enhanced photoexcitation can further increase the density of triplet excitons to improve the spin current, and thus leads to a high voltage generation or a high magnetoelectric coupling coefficient (Figure 3d).

The relatively low conductivity in magnetic BCCTs and magnetic-field-dependent capacitance can exclude the possibility of an inverse spin Hall effect here.[17] Though magnetoresistance (magnetoconductance) is observed in BCCTs, it is independent of the direction of the magnetic-field vector.[17] Furthermore, the observed magnetocapacitance without loading external electric field eliminates the magnetoresistance effect here. In addition, the Nernst effect is not relevant here for the observed voltage generation due to the low conductivity of BCCTs.[18] Besides, the light-intensity-dependent tendency excludes the possibility of electromagnetic-induced current. Magnetic-field effects and spin–charge conversion are responsible for the generation of charge in organic BCCT materials without loading of an external electric field.[19] A saturation magnetization of ≈69.2 emu per mole with a spin density of 11.5% along the horizontal orientation is observed in BCCTs, suggesting their magnetic characteristics (Figure S6, Supporting Information). As shown in Figure 3e,f, magnetoconductance (MC) was measured to gain further understanding of the spin–charge interactions and magnetoelectric coupling, where the BCCTs demonstrate an enhanced MC effect with the increase of magnetic-field or light intensity. As discussed above, a magnetic field can induce intersystem crossing from singlet to triplet CT with an increase in the density of polarons and triplet excitons. The interaction between polarons and triplet excitons leads to the dissociation of triplet excitons into free charge carriers with an increase in current density. The increased magnetic field or photoexcitation enhanced MC could therefore further confirm the magnetoelectric effect and spin–charge interactions. The

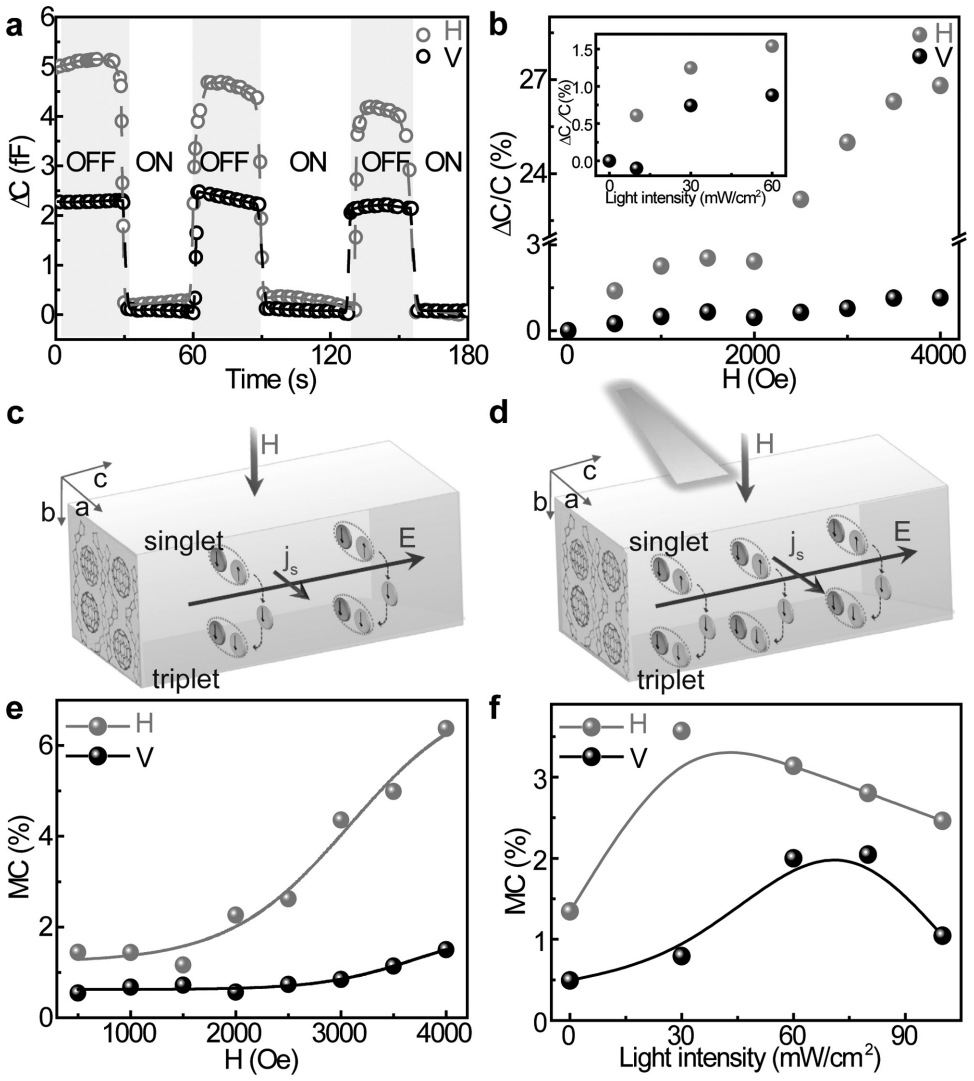

Figure 3. a) Magnetocapacitance change for horizontal and vertical orientations with an external magnetic field of 4000 Oe. b) Magnetic-field-dependent magnetocapacitance change for horizontal and vertical orientations. The inset is the light-intensity-dependent capacitance change for horizontal and vertical orientations. c,d) The possible mechanism for magnetic-energy harvesting and magnetoelectric coupling in BCCTs. The intersystem crossing by external magnetic field induces spin current, and the coupling of spin current and external magnetic field generates electrical potential difference along the horizontal orientation of the crystals. e) Magnetic-field-dependent magnetoconductance (MC) for horizontal and vertical orientations, respectively. f) MC under dark and light of horizontal orientation. The light intensity is 120 mW cm^{-2}.

self-powered flexible sensing devices based on BCCTs represent a significant step toward the development of sustainable sensors. For the BCCT device systems, magnetic-field sensing can be accomplished without an additional power supply, because their output voltage or current is an additional read-out signal generated by magnetic-energy harvesting.

In order to understand the nature of CT in BCCT crystals, we performed first principle DFT calculations. The electronic density of states (DOS) and the partial density of states (PDOS) are shown in **Figure 4**a,b for the BCCT, BEDT-TTF, and C_{60} crystals, respectively. The energies are shifted by the respective Fermi energy. The highest occupied molecular orbital (HOMO) and lowest unoccupied molecular orbital (LUMO) of the BCCT crystal overlap to a good approximation with those of the BEDT-TTF and C_{60} crystals, respectively. Addition of BEDT-TTF to the C_{60} crystal results in shifting of the HOMO level closer to the Fermi energy, thereby decreasing the HOMO–LUMO gap of the complex, and thus contributing to the charge transfer from BEDT-TTF to C_{60}. The HOMO is comprised mainly of the 2p states of S atoms in BEDT-TTF, while the 2p states of C atoms in the C_{60} molecules dominate the LUMO band (Figure 4b). This suggests that charge transfer is occurring between the *n*-orbitals of the S atoms in BEDT-TTF and the π^* orbitals of C_{60}, as previously predicted.[20] Other CT pathways of lower probability may also exist; the PDOS shows significant density of BEDT-TTF C atom 2p states in the HOMO, supporting the possibility of a π to π^* transition between BEDT-TTF and C_{60}. Intermolecular charge transfer in this manner results in spatial separation of charge in the CT state, with accumulation of holes on the BEDT-TTF molecules and electrons on the C_{60} molecules.

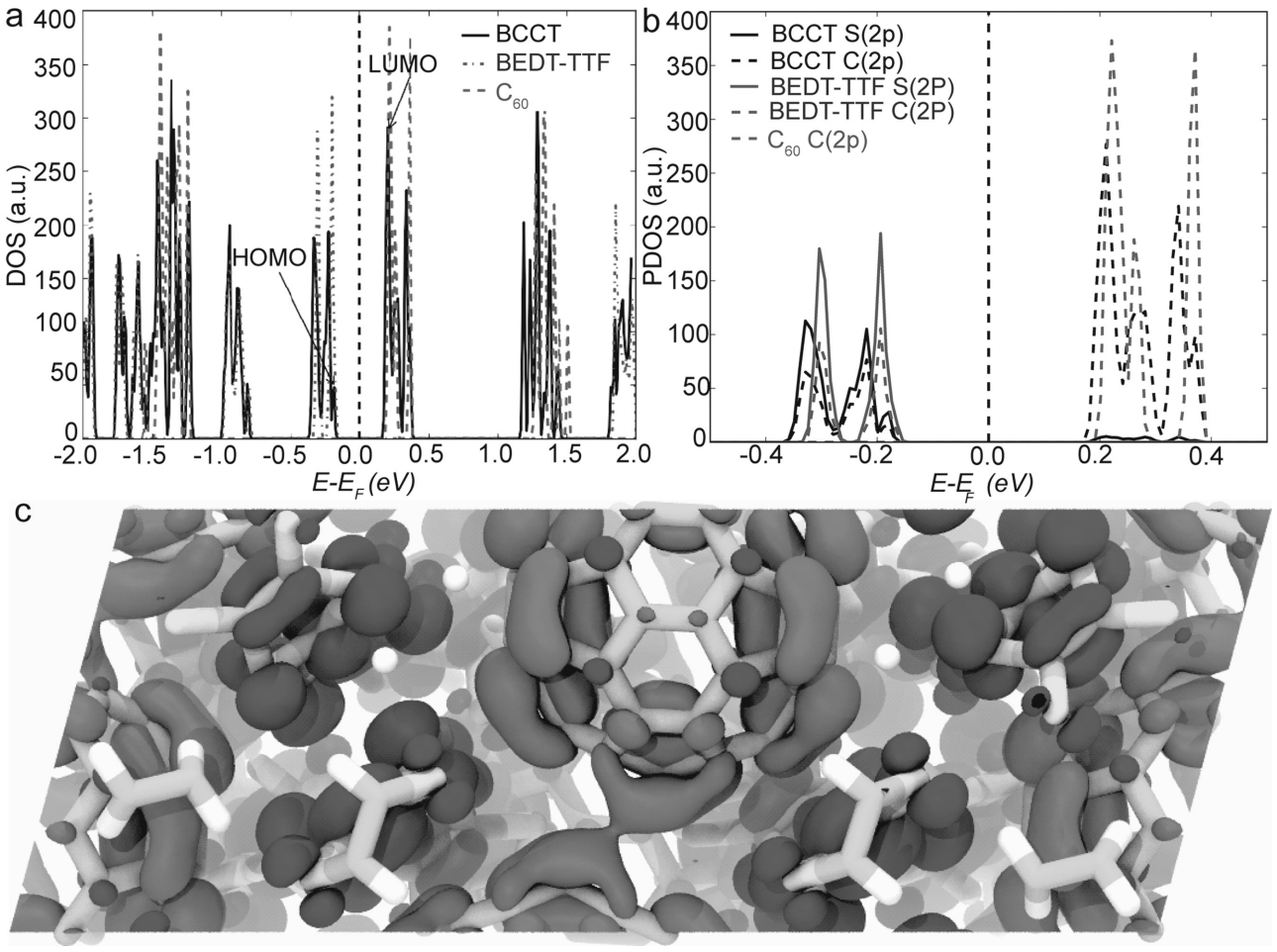

Figure 4. a) Electronic density of states (DOS) plots. Solid curve denotes the DOS of BCCT crystal, dashed curve for C_{60}, and dotted curve for BEDT-TTF. The energies have been shifted with respect to their Fermi energies. b) Partial density of states (PDOS) plots of BCCT, BEDT-TTF, and C_{60} crystals. The solid and dashed curves denote the PDOS for 2p orbitals of S and C atoms, respectively. The energies have been shifted with respect to their Fermi energies. c) Charge density isosurface of the HOMO and LUMO bands of BCCT.

This is evidenced by the charge density isosurfaces of the HOMO and LUMO states in Figure 4c. The spatial distributions of these states additionally support the above conclusion that proximity of the HOMO and LUMO in the crystal growth direction enhances charge transport with respect to other directions along the crystal.

To evaluate the self-powered and simultaneous sensing abilities of BCCTs, we constructed flexible devices by integrating free-standing crystals with a poly(dimethylsiloxane) (PDMS) substrate (**Figure 5**a). Because of the voltage or current generation from the magnetic energy, magnetic-field sensing from any ac current source can be accomplished simultaneously without an additional power supply. The BCCT devices demonstrate a repeatable and linear current change response to a magnetic field generated from the ac current I with a frequency of 0.5 Hz, as the current sensor (Figure 5b,c). The self-powered and reliable current sensors constructed from molecular CT crystals could be beneficial and efficient for detecting the electrical currents in electrical cables or conductors, in comparison to the traditional current sensors based on Hall sensors or reluctance coils.

The BCCT-based flexible devices developed here not only can be utilized as electricity generators, but they also switch to a stimuli-sensing model by introducing either temperature or pressure (Figure 5d–i). This novel wearable element mimics functional electronic skin and next-generation artificial intelligence relies on the simultaneous sensing of temperature and pressure stimuli.[1a] To evaluate the temperature sensor applications of BCCTs for the monitoring of skin temperature, the temperature-dependent current–voltage curves are examined near room temperature (20–70 °C) (Figure 5d). The current density of BCCT flexible devices increases dramatically with increasing temperature. The inset of Figure 5d demonstrates a negative resistor temperature-sensing characteristic of BCCTs. The response of resistance with temperature is calculated by $(\Delta R/R_0) \times 100\%$, where ΔR is the resistance change between a set temperature and 20 °C, and R_0 is the resistance at 20 °C. The resistance–temperature sensitivity is ≈1.54% $°C^{-1}$, which is close to the flexible temperature sensor for electronic skin applications.[2,21] The linear response of resistance to temperature is due to the small temperature range used here. The

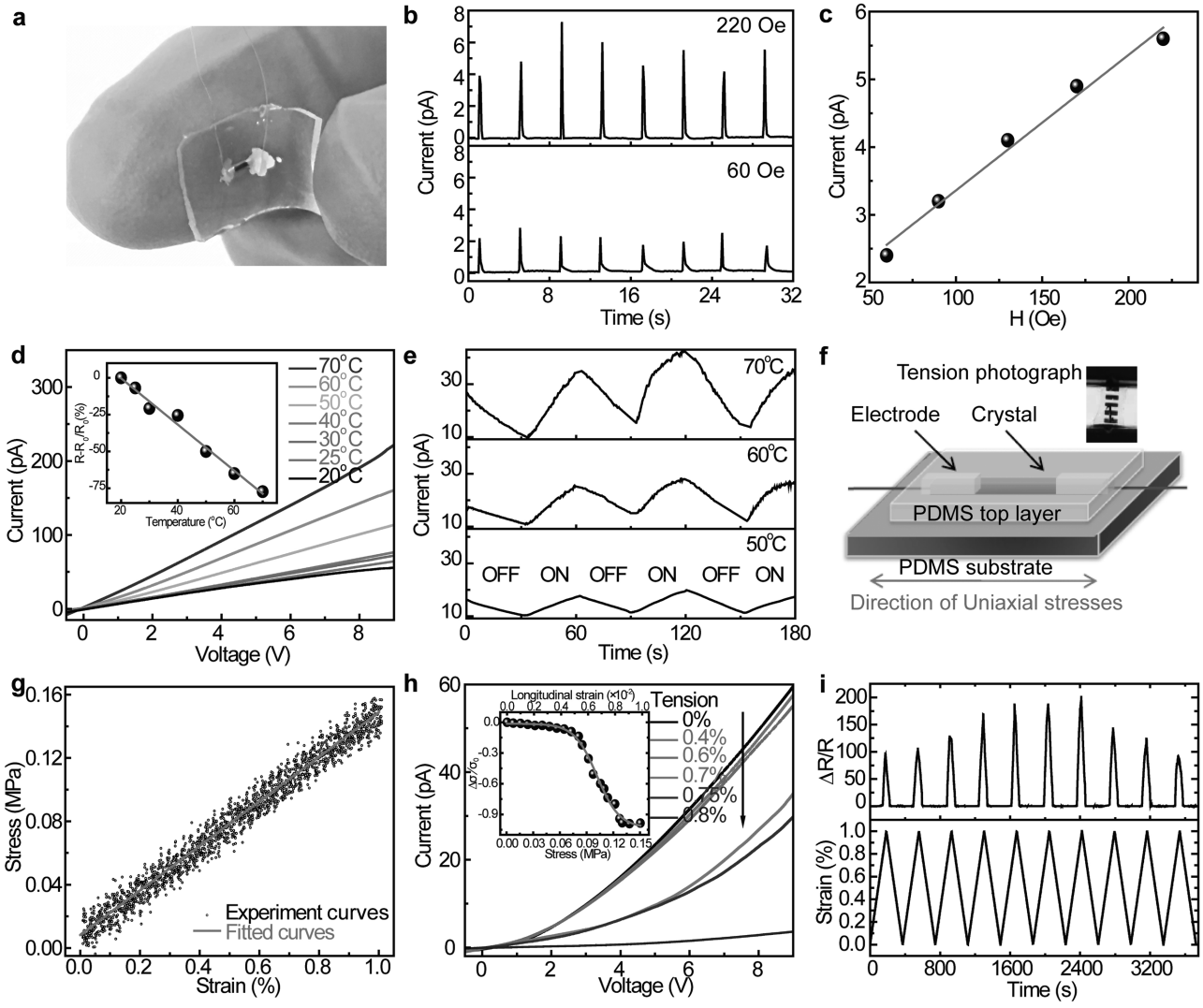

Figure 5. a) The photograph of flexible crystals on PDMS substrate. b) Current sensor of BCCTs at an output magnetic field of 60 and 220 Oe by vortex wire coil. c) The relationship between the output magnetic field of vortex wire coil and output current by BCCTs. d) Temperature-dependent current–voltage curves of BCCTs. The inset is the temperature-dependent resistance change. e) The current change of BCCTs with the heat on/off at different temperatures. f) The scheme of the pressure sensor made by BCCTs and PDMS. g) Strain–stress curves for the pressure sensor. h) Tension strain-dependent current–voltage curves. The inset is the strain–stress-dependent conductivity change of the pressure sensor. i) Resistance change with time upon ten cycles of uniaxial tension stress at a rate of 1.0 μm s^{-1} along the horizontal orientation of BCCTs.

conductivity–temperature relationship has some deviation from a Boltzmann-like activation process and cannot be fit by Mott and Efros–Shklovskii hopping conduction processes (Figure S18, Supporting Information).[22] To assess the recycling behavior and the response rate to heat, the BCCT devices were attached to a heat source under the loading and unloading cycles at different temperatures (Figure 5e). They show perfect repeatable behavior and response time within several seconds, demonstrating the potential for actual thermal-sensing applications.

Generally, physical or chemical pressure can finely tune the ground state of the BEDT-TTF family with a superconduction transition under a low pressure of ≈300 bar for κ-(BEDT-TTF)2Cu[$N(CN)_2$]Cl.[8] To demonstrate the pressure-sensing ability of BCCTs, the conductivity change by tension strain along the crystal growth direction is examined. The structure of the flexible BCCT devices and the measurement scheme are illustrated in Figure 5f and Figure S18a (Supporting Information), respectively. The stress–strain follows a linear relationship, indicating that no permanent damage is accumulated in the crystals (Figure 5g). In the range of strain from 0% to 0.8%, the current density decreases dramatically with the loading of strain and the current recovers after unloading the strain (Figure 5h and Figure S19b (Supporting Information)). For a large conductivity change, the piezoresistance coefficient is defined as:

$$\pi^{\sigma} = \frac{1}{X}\frac{\Delta\sigma}{\sigma_0} \quad (1)$$

where $\Delta\sigma$ and σ_0 are the conductivity change and conductivity without strain, X is the stress.[22,23] The piezoresistance coefficient of BCCTs is nonlinear, where the conductivity change reaches –0.99% under a strain of 0.98%.[24] Under a low strain, the piezoresistance coefficient is -5.7×10^{-7} Pa^{-1}, and it increases to -5.1×10^{-6} Pa^{-1} under a high strain, which is significantly higher than that of the reported giant piezoresistance nanowires,[24] and comparable to that of Sr_2IO_4 thin film,[25] making the emergence of BCCTs as a new generation of giant piezoresistance organic CT materials. The influence of repetitive strain on the piezoresistance properties is examined by cyclic loading and unloading of strain as shown in Figure 5i. The resistance demonstrates a periodic change with the cyclic strain change, with the highest increase of 200 times under a strain of 1%. The gauge factor is another way to explain the value of strain sensitivity, defined as $\frac{\Delta R}{R_0\varepsilon}$, where ΔR is the resistance change under strain and without strain, R_0 is the resistance without strain, ε is the strain. We note that the response to stress is not stable after cycling several times due to the fragility of organic crystals. Nevertheless, the gauge factor reaches the highest value of 200, which is much larger than that of α-(BEDT-TTF)$_2$I$_3$ crystals.[6] The large sensitivity of BCCTs might result from the tuning of π–π stacking interactions with the change of charge density along the crystal growth direction by the tension strain. It is worth noting that the sensitivity and response time of BCCT-based CT flexible devices can meet the requirement of many electronic skin and artificial intelligence systems. More importantly, the BCCT devices also exhibit energy harvesting and excellent stability, and the combination of all these properties makes BCCT crystals applicable as integrated energy-harvesting–sensing elements.

We have demonstrated the ability of centimeter-sized molecular CT crystals to simultaneously perform magnetic-field energy harvesting and external-stimuli-responsive-sensing. Preferred growth of these crystals along the π–π stacking direction leads to anisotropic BCCT properties. We also explored the magnetic-field- and light-intensity-dependent magnetoconductance and magnetocapacitance to uncover the possible mechanism of magnetic-field energy harvesting. From this, we propose that the generation of spin current via intersystem crossing from a singlet to a triplet charge-transfer state and coupling with an external magnetic field contributes to the generated voltage and current in BCCTs. The combination of spin–charge interactions, plus magnetoelectric and piezoresistance mechanisms enables a self-powered magnetic-field sensor and temperature–pressure detector, with a large resistance–temperature sensitivity of ≈1.5% K^{-1} and giant piezoresistance coefficient of -5.1×10^{-6} Pa^{-1}. DFT calculations indicate that the HOMO–LUMO gap of BCCTs is dramatically decreased in comparison to the single donor or acceptor components and confirm strong charge transfer in these crystals. The present work holds promise for an alternative magnetic-energy-harvesting strategy using organic charge-transfer crystals instead of traditional magnetoelectric oxides. Our findings also suggest a way to meet the critical demands of multisensing elements for healthcare and artificial intelligence products.

Experimental Section

The preparation strategy for the crystals and the flexible devices, the computational details are presented in the Supporting Information. A Bruker Apex II Duo single-crystal X-ray diffractometer was used to obtain the XRD pattern at a step of 0.02° per step from 5° to 35°. A CHI 422 Series Electrochemical Workstation was used to capture the current and voltage signals. A Helmholtz coil was used to output magnetic field with a period of 2 or 30 s with the largest output of 400 mT. A Driel's 50–150 W Research Arc Lamp Sources with different powers of simulated solar light was used as the light source. The capacitance measurements were performed on an Agilent 4294a Precision impedance equipment with a frequency between 40 and 10 MHz. The voltage was 0.5 V. For the current sensor, the magnetic field was generated by a vortex electromagnetic coil with the output magnetic field from 60 to 220 Oe. For the temperature sensor, a hot plate was used as the thermal source. A thermometer was used to calibrate the temperature. For the pressure sensor, an Instron 5944 Single Column Tabletop Low-Force Universal Testing System with a speed of 1.0 μm s^{-1} was used to apply tension strain to the samples.

The calculations were based on first-principle DFT as implemented in the Quantum ESPRESSO code.[26] A generalized gradient approximation was used with the Perdew–Burke–Ernzerhof[27] parameterization of exchange correlation energy functional with ultrasoft pseudopotentials.[28] An energy cut-off of 30 Ry was used for truncating the plane wave basis set to represent wave functions. The structures were relaxed till the magnitude of the Hellman–Feynman force on each ion became smaller than 0.03 eV Å^{-1}. Brillouin zone integrations were carried out with a uniform small mesh of k-points. Van der Waals interactions were included using parameterization of Grimme.[29] For the purpose of this study, the crystal structure of BEDT-TTF–C_{60} complex ((BEDT-TTF)$_2C_{60}$) from the Cambridge Crystallographic Data Centre was used. The crystal structures of BEDT-TTF and C_{60} were also used, formed by removing the structures of C_{60} and BEDT-TTF, respectively, from those of the complex.

Supporting Information

Supporting Information is available from the Wiley Online Library or from the author.

Acknowledgements

Work at the Temple University (S.R.) was supported by the Army Research Office-Young Investigator Program (W911NF-15-1-0610, material design/self-assembly), the U.S. Department of Energy-Basic Energy Sciences Award No. DE-SC0014902 (organic synthesis and physical property measurement). H.C., R.C.R., and part of the computational resources were supported as part of the Center for the Computational Design of Functional Layered Materials, an Energy Frontier Research Center funded by the U.S. Department of Energy, Office of Science, Basic Energy Sciences under Award #DE-SC0012575. A portion of the computations was performed on resources provided by the National Science Foundation through major research instrumentation grant number CNS-09-58854. H.C., R.C.R., and M.L.K. also acknowledge discussions and interactions with Prof. U. V. Waghmare.

Received: September 23, 2016
Revised: November 7, 2016
Published online:

[1] a) F. Zhang, Y. Zang, D. Huang, C.-A. Di, D. Zhu, *Nat. Commun.* **2015**, *6*, 8356; b) D.-H. Kim, N. Lu, R. Ghaffari, Y.-S. Kim, S. P. Lee, L. Xu, J. Wu, R.-H. Kim, J. Song, Z. Liu, J. Viventi, B. de Graff,

B. Elolampi, M. Mansour, M. J. Slepian, S. Hwang, J. D. Moss, S.-M. Won, Y. Huang, B. Litt, J. A. Rogers, *Nat. Mater.* **2011**, *10*, 316; c) Z. L. Wang, W. Wu, *Angew. Chem., Int. Ed.* **2012**, *51*, 11700.

[2] J. Park, M. Kim, Y. Lee, H. S. Lee, H. Ko, *Sci. Adv.* **2015**, *1*, e1500661.

[3] J. Ma, Z. Shi, C.-W. Nan, *Adv. Mater.* **2007**, *19*, 2571.

[4] a) J. Ryu, J.-E. Kang, Y. Zhou, S.-Y. Choi, W.-H. Yoon, D.-S. Park, J.-J. Choi, B.-D. Hahn, C.-W. Ahn, J.-W. Kim, Y.-D. Kim, S. Priya, S. Y. Lee, S. Jeong, D.-Y. Jeong, *Energy Environ. Sci.* **2015**, *8*, 2402; b) C.-W. Nan, M. I. Bichurin, S. Dong, D. Viehland, G. Srinivasan, *J. Appl. Phys.* **2008**, *103*, 031101; c) N. Cui, W. Wu, Y. Zhao, S. Bai, L. Meng, Y. Qin, Z. L. Wang, *Nano. Lett.* **2012**, *12*, 3701; d) J. Zhai, Z. Xing, S. Dong, J. Li, D. Viehland, *Appl. Phys. Lett.* **2006**, *88*, 062510; e) Y. Zhou, D. J. Apo, S. Priya, *Appl. Phys. Lett.* **2013**, *103*, 192909.

[5] a) H. Miyasaka, *Acc. Chem. Res.* **2013**, *46*, 248; b) T. Yamamoto, *NPG Asia Mater.* **2010**, *2*, 54; c) W. Qin, B. Xu, S. Ren, *Nanoscale* **2015**, *7*, 9122; d) B. Xu, H. Li, A. Hall, W. Gao, M. Gong, G. Yuan, J. Grossman, S. Ren, *Sci. Adv.* **2015**, *1*, e1501264; e) A. K. S. A. Tayi, A. Sue, J. Szarko, B. Rolczynski, D. Cao, T. Kennedy, A. Sarjeant, C. Stern, W. Paxton, W. Wu, S. Dey, A. Fahrenbach, J. Guest, H. Mohseni, L. Chen, K. Wang, J. F. Stoddart, S. I. Stupp, *Nature* **2012**, *488*, 485.

[6] E. Steven, V. Lebedev, E. Laukhina, C. Rovira, V. Laukhin, J. S. Brooks, J. Veciana, *Mater. Horiz.* **2014**, *1*, 522.

[7] P. Lunkenheimer, J. Muller, S. Krohns, F. Schrettle, A. Loidl, B. Hartmann, R. Rommel, M. de Souza, C. Hotta, J. A. Schlueter, M. Lang, *Nat. Mater.* **2012**, *11*, 755.

[8] M. Suda, Y. Kawasugi, T. Minari, K. Tsukagoshi, R. Kato, H. M. Yamamoto, *Adv. Mater.* **2014**, *26*, 3490.

[9] G. Saito, T. Murata, *Philos. Trans. R. Soc., A* **2008**, *366*, 139.

[10] K. P. Goetz, A. Fonari, D. Vermeulen, P. Hu, H. Jiang, P. J. Diemer, J. W. Ward, M. E. Payne, C. S. Day, C. Kloc, V. Coropceanu, L. E. McNeil, O. D. Jurchescu, *Nat. Commun.* **2014**, *5*, 5642.

[11] S.-L. Cai, Y.-B. Zhang, A. B. Pun, B. He, J. Yang, F. M. Toma, I. D. Sharp, O. M. Yaghi, J. Fan, S.-R. Zheng, W.-G. Zhang, Y. Liu, *Chem. Sci.* **2014**, *5*, 4693.

[12] J. Ma, J. Hu, Z. Li, C. Nan, *Adv. Mater.* **2011**, *23*, 1062.

[13] S. Ren, M. Wuttig, *Adv. Mater.* **2012**, *24*, 724.

[14] B. Hu, L. Yan, M. Shao, *Adv. Mater.* **2009**, *21*, 1500.

[15] W. Qin, M. Gong, T. Shastry, M. C. Hersam, S. Ren, *Sci. Rep.* **2014**, *4*, 6126.

[16] L. He, M. Li, A. Urbas, B. Hu, *Adv. Mater.* **2014**, *26*, 3956.

[17] K. Ando, S. Watanabe, S. Mooser, E. Saitoh, H. Sirringhaus, *Nat. Mater.* **2013**, *12*, 622.

[18] G. E. W. Bauer, E. Saitoh, B. J. van Wees, *Nat. Mater.* **2012**, *11*, 391.

[19] Y. Zheng, F. Wudl, *J. Mater. Chem. A* **2014**, *2*, 48.

[20] a) T. T. Akira Izuoka, T. Sugawara, Y. Suzuki, M. Konno, Y. Saito, H. Shinohara, *J. Chem. Soc., Chem. Commun.* **1992**, 1472; b) B. Xu, W. Gao, A. J. Wilson, C. He, X. Chen, G. Yuan, H. Dai, Y. Rao, K. Willets, Z. Dauter, S. Ren, *Chem. Mater.* **2016**, *28*, 2441.

[21] T. Q. Trung, S. Ramasundaram, B.-U. Hwang, N.-E. Lee, *Adv. Mater.* **2016**, *28*, 502.

[22] Y. Singh, *AIP Conf. Proc.* **2013**, *1536*, 1334.

[23] W. P. Mason, R. N. Thurston, *J. Acoust. Soc. Am.* **1957**, *29*, 1096.

[24] R. He, P. Yang, *Nat. Nanotechnol.* **2006**, *1*, 42.

[25] N. Domingo, L. Lopez-Mir, M. Paradinas, V. Holy, J. Zelezny, D. Yi, S. J. Suresha, J. Liu, C. Rayan Serrao, R. Ramesh, C. Ocal, X. Marti, G. Catalan, *Nanoscale* **2015**, *7*, 3453.

[26] P. Giannozzi, S. Baroni, N. Bonini, M. Calandra, R. Car, C. Cavazzoni, D. Ceresoli, G. L. Chiarotti, M. Cococcioni, I. Dabo, A. Dal Corso, S. de Gironcoli, S. Fabris, G. Fratesi, R. Gebauer, U. Gerstmann, C. Gougoussis, A. Kokalj, M. Lazzeri, L. Martin-Samos, N. Marzari, F. Mauri, R. Mazzarello, S. Paolini, A. Pasquarello, L. Paulatto, C. Sbraccia, S. Scandolo, G. Sclauzero, A. P. Seitsonen, A. Smogunov, P. Umari, R. M. Wentzcovitch, *J. Phys.: Condens. Matter* **2009**, *21*, 395502.

[27] J. P. Perdew, K. Burke, M. Ernzerhof, *Phys. Rev. Lett.* **1996**, *77*, 3865.

[28] D. Vanderbilt, *Phys. Rev. B* **1990**, *41*, 7892.

[29] S. Grimme, *J. Comput. Chem.* **2009**, *27*, 1787.